

# MOF-derived iron as an active energy storage material for intermediate-temperature solid oxide iron-air redox battery

*Cuijuan Zhang<sup>\*a,b</sup> and Kevin Huang<sup>\*a</sup>*

<sup>a</sup> Department of Mechanical Engineering, University of South Carolina, Columbia, SC, USA  
29208

<sup>b</sup> School of Chemical Engineering and Technology, Tianjin University, Tianjin, China 300350

Corresponding Author: HUANG46@cec.sc.edu; cjzhang@tju.edu.cn

## Experimental Methods

**Synthesis of MIL-88B (Fe):** A typical iron-based MOF, MIL-88B(Fe) was chosen as the template to prepare Fe<sub>2</sub>O<sub>3</sub>. The MIL-88B(Fe) was synthesized by solvothermal method following the procedure in reference<sup>1</sup> with a slight modification. Briefly, 2.046 g FeCl<sub>3</sub>·6H<sub>2</sub>O (97%, Sigma-Aldrich) and 1.260 g terephthalic acid (98+%, Alfa Aesar) were dissolved in 160 ml N,N-Dimethylformamide (DMF, ACS 99.8+%, Alfa Aesar) at room temperature and then transferred to Teflon-lined stainless steel autoclave of 200 ml and heated at 110 °C for 48 h in a drying oven. After cooling down to room temperature naturally, the orange product was collected by centrifugation and washed with DMF for four times. Finally, the sample was dried at 80 °C for 12 h.

**Preparation of Fe<sub>2</sub>O<sub>3</sub>:** A two-step calcination method<sup>2</sup> was utilized to prepare Fe<sub>2</sub>O<sub>3</sub>. The MIL-88B(Fe) powders were first annealed at 550 °C for 1 h in flowing argon (100 sccm) at the heating rate of 10 °C min<sup>-1</sup> in a tubular furnace. The resultant black powder was then calcined at 550 °C for 1 h in air in a muffle furnace at the same heating rate, leading to the final product, which is used for subsequent battery test.

**Battery test:** The details of the preparation of the anode-supported SOFC and assembling and test of battery can be found in our very recent reports.<sup>3,4</sup> A 0.0786 g Fe<sub>2</sub>O<sub>3</sub> powder was loaded as ESU material. The battery was tested at 500 °C. Various discharge/charge current densities (*C*/5.5, *C*/5, *C*/4, *C*/3) and iron utilization (*U*<sub>Fe</sub>, 3-80%) (Table S1) was applied and the corresponding voltage response was recorded. All the tests were performed on a Solartron electro-chemical station consisting of a 1470 multichannel potentiostat and a 1255B frequency response analyser.

**Characterization:** The crystal structure of MIL-88B(Fe) and iron oxide was examined by X-ray diffraction (XRD, Rigaku Miniflex II X-ray powder diffractometer) with Cu K $\alpha$  radiation. Field-

emission scanning electron microscope (FE-SEM, Zeiss Ultra plus) was employed to detect the microstructure of MIL-88B(Fe), fresh and tested ESU materials. The microstructure of fresh Fe<sub>2</sub>O<sub>3</sub> was also characterized by transmission electron microscopy (TEM, Hitachi 9500) with an acceleration voltage of 300 kV. The powder was dispersed in ethanol onto carbon film coated copper grids before TEM observation. The Fe<sub>2</sub>O<sub>3</sub> powders were degassed at 300 °C for 1 h under vacuum before the N<sub>2</sub> sorption analysis was run at 77 K.

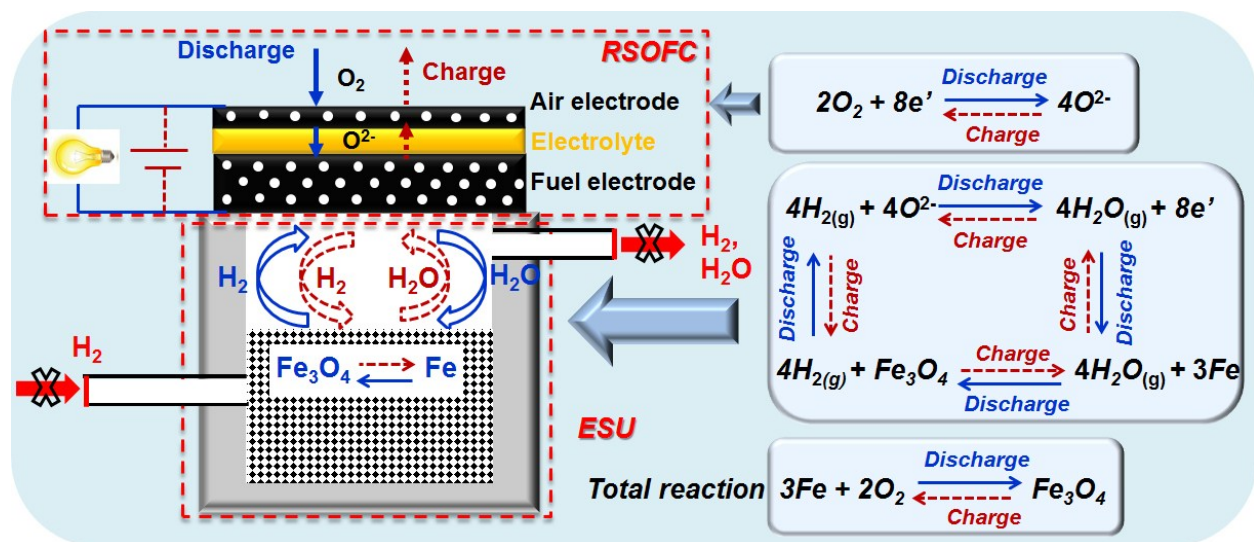


**Fig. S1.** Schematic of components and working principle of SOIARB at 500-600 °C. The solid and dashed arrows represent the discharge and charge cycles, respectively.

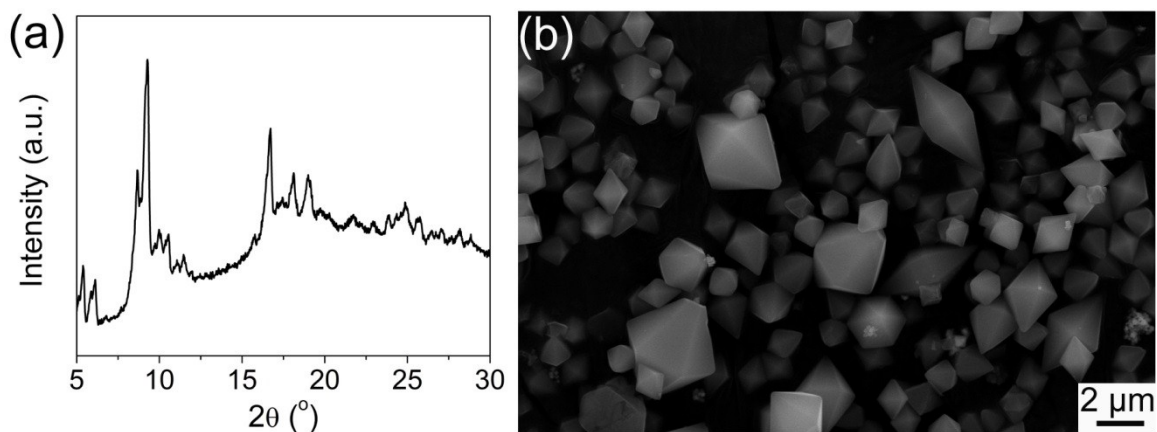


**Fig. S2.** (a) XRD pattern and (b) SEM image of as-obtained MIL-88(B)Fe.

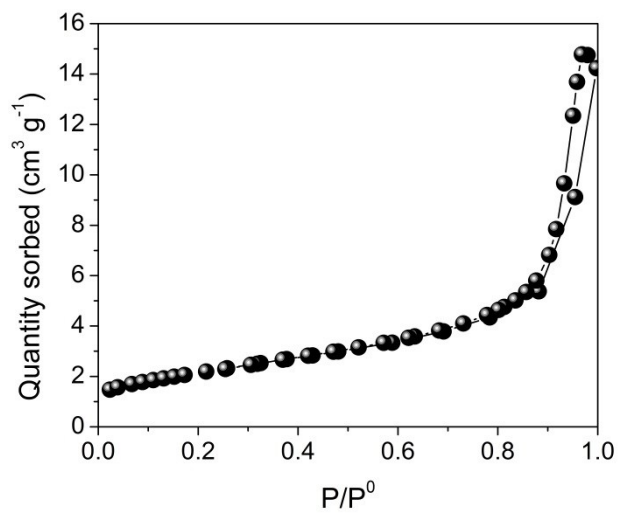


**Fig. S3.** Nitrogen sorption isotherms of the fresh Fe<sub>2</sub>O<sub>3</sub> oxide powder.

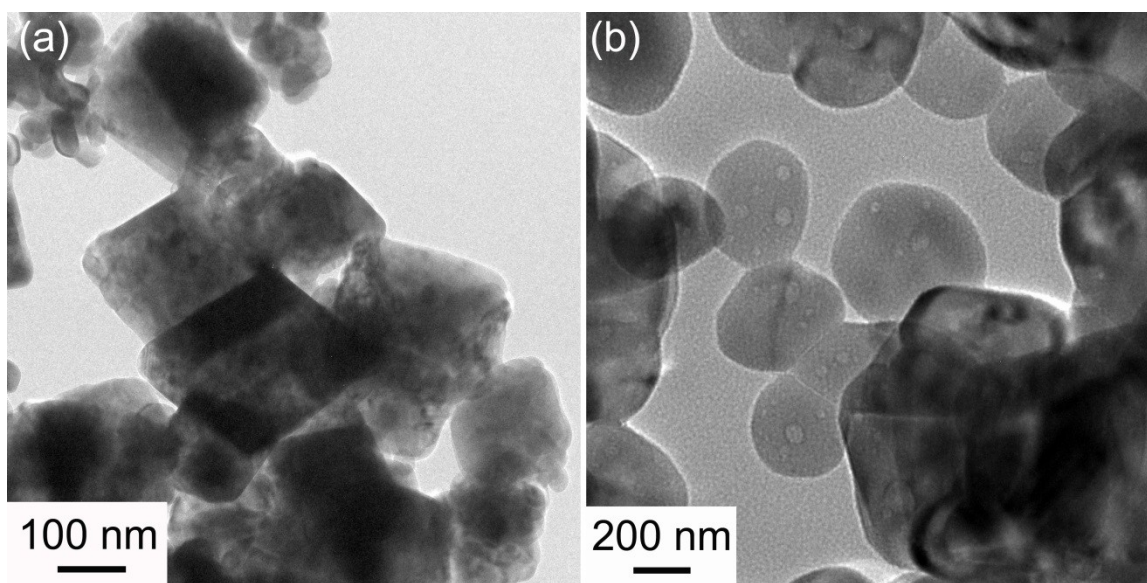


**Fig. S4.** TEM images of  $\alpha$ -Fe<sub>2</sub>O<sub>3</sub> particles.

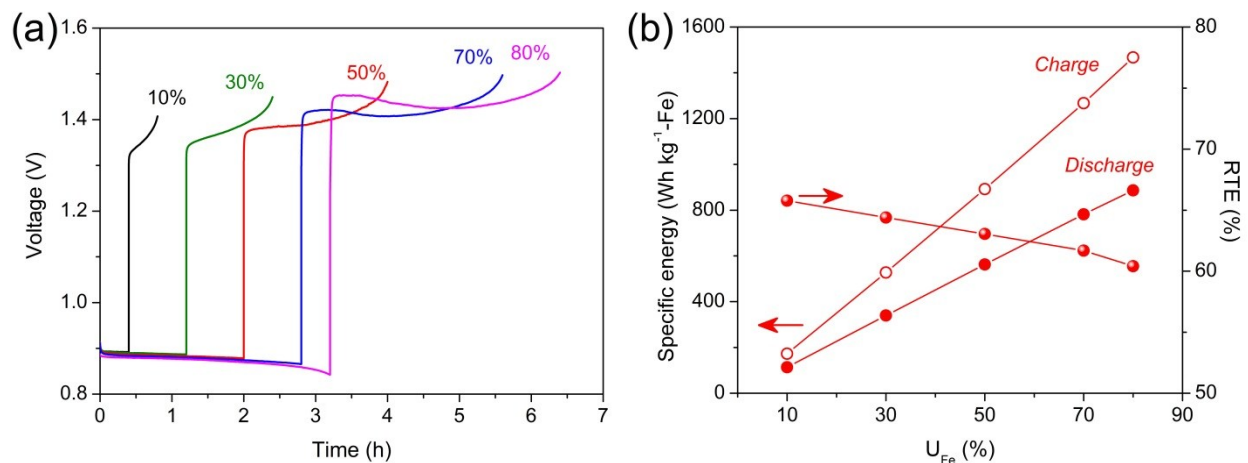


**Fig. S5.** (a) Voltage profile vs. time and (b) discharge and charge mass specific energy and round trip efficiency (RTE) vs. iron utilization ( $U_{Fe}$ ) for battery operated at  $C/4$  and  $500\text{ }^{\circ}\text{C}$ . The cut-off voltage is set to be 0.8 and 2.0 V for the discharge and charge cycles, respectively, to prevent the oxidation of Ni in the RSOFC anode and the decomposition of zirconia-based electrolyte.<sup>5</sup> The battery can cycle at a  $U_{Fe}$  ranging from 10 to 80%. Both discharge and charge mass-specific energy increase with  $U_{Fe}$  as expected, e.g., 113.5, 562.4, and 886.3 Wh kg<sup>-1</sup>-Fe at  $U_{Fe} = 10\%$ , 50%, and 80%, respectively. Since the charge mass-specific energy increases with  $U_{Fe}$  faster than the discharge, it results in a decrease of RTE from 65.8% at  $U_{Fe} = 10\%$  to 60.4% at  $U_{Fe} = 80\%$ .

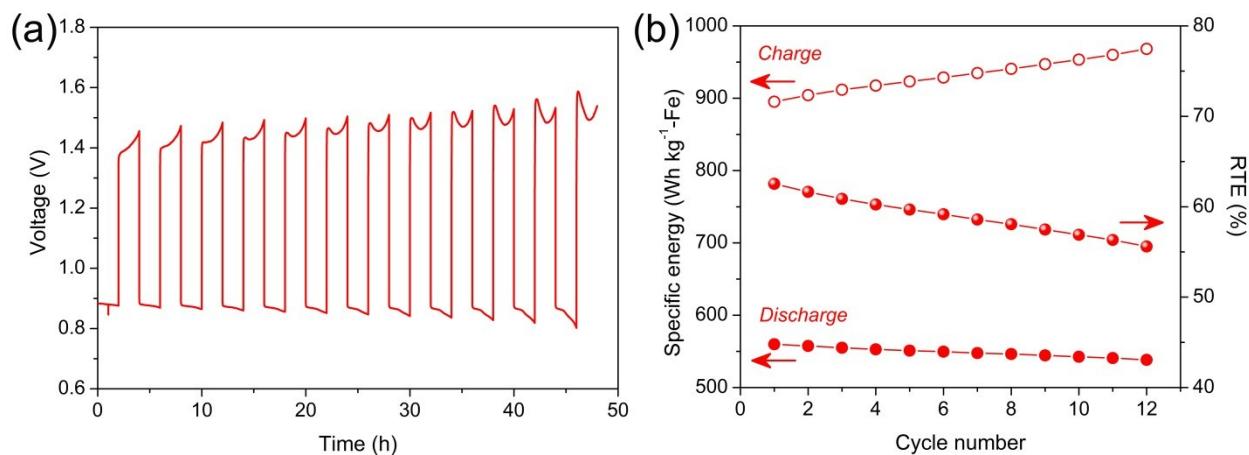


**Fig. S6.** (a) Voltage profile vs. time and (b) discharge and charge mass specific energy and round trip efficiency (RTE) vs. cycle number for battery operated at  $C/4$  and  $U_{Fe} = 50\%$ . Over the 12 cycles achieved, an interesting observation is the voltage variation within each charging cycle: increasing with time in the first 2 cycles, then reaching a minimum in subsequent cycles. Such phenomenon has also been observed in our previous work.<sup>6</sup> The exact reasons remain unclear, but it is likely associated with the microstructural change in ESU materials, probably induced by sintering. Compared with previous baseline  $Fe_2O_3-ZrO_2$ ,<sup>6</sup> no sintering inhibitor (e.g.,  $ZrO_2$ ) was added to MOF- $Fe_2O_3$  in this work. Indeed, the nano and sub-micro sized iron metal particles are prone to sinter, which could lead to a faster degradation rate. In this case, the battery delivers an average discharge mass specific energy of  $548.8 \pm 6.4$  Wh kg<sup>-1</sup>-Fe with a RTE of  $58.1 \pm 2.1\%$  for 12 cycles.

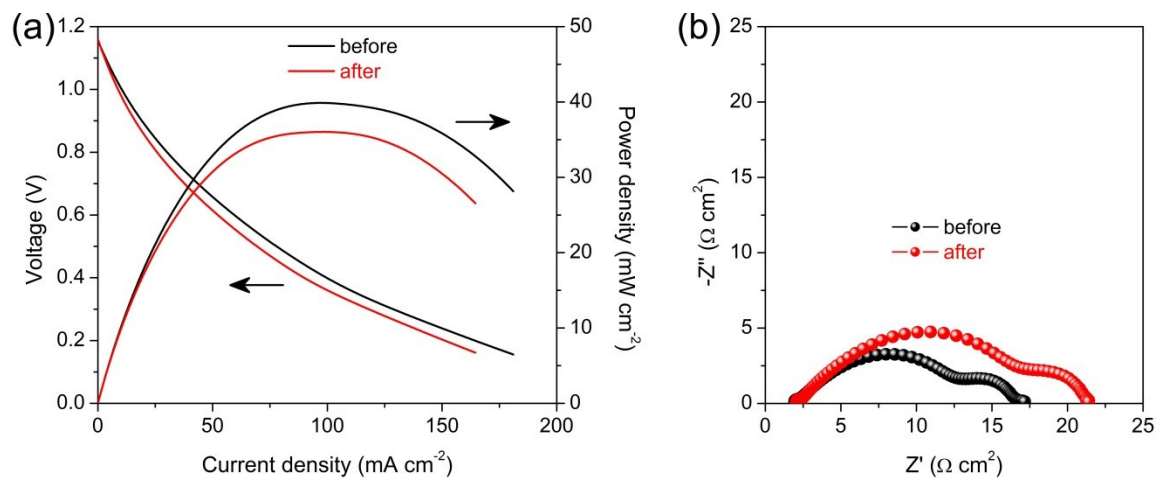


**Fig. S7.** (a) Current-voltage and current-power density curves and (b) AC impedance spectra of RSOFC at 500 °C **before** any battery test, and **after** battery cycling and regeneration. Wet hydrogen ( $\sim 3\%$   $\text{H}_2\text{O}$ ) and static air are the fuel and oxidant, respectively. The power output decreases and electrode polarization, especially the anode polarization,<sup>6</sup> increases after cycling. Such degradation of RSOFC can increase the discharge and charge energy losses during cycling and thus reduce RTE.

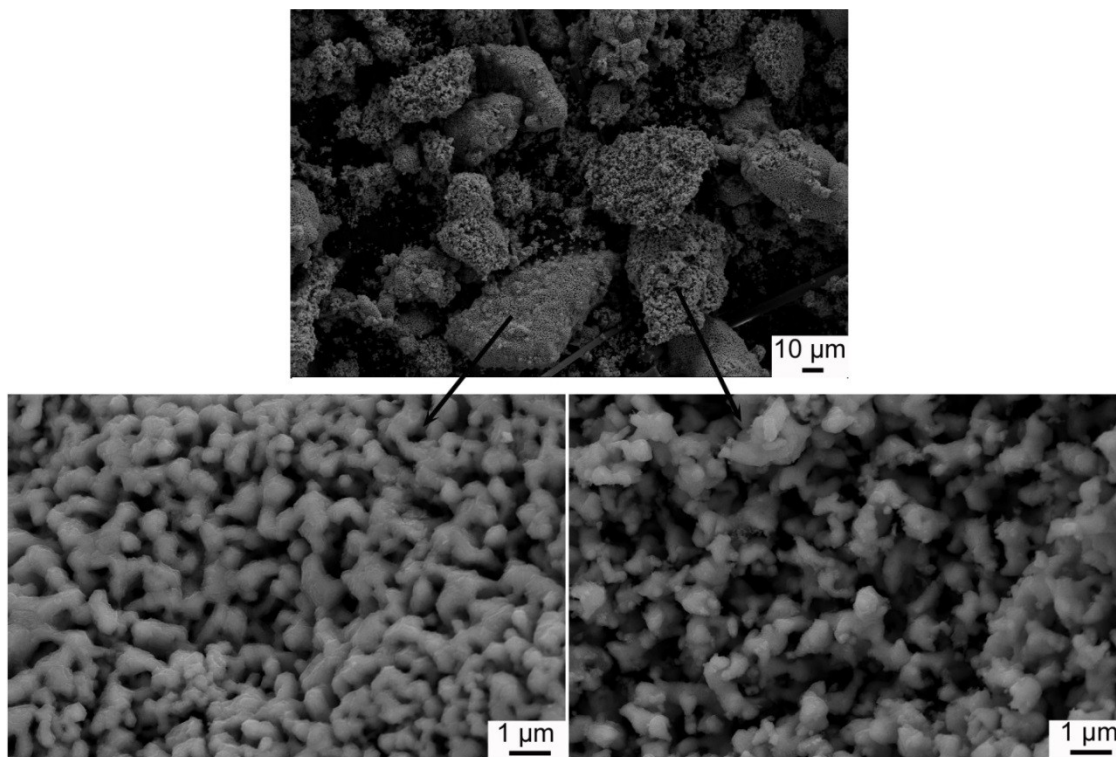


**Fig. S8.** Typical SEM images of ESU materials after battery test. A serious iron sintering has taken place, which has inevitably reduced the effective reaction sites and impeded the diffusion of  $H_2$  and steam through the scale during cycling, also leading to a decreased RTE. Improving the sintering resistance of MOF-Fe will be the focus of our future work.

**Table S1.** C-rate, current density and iron utilization ( $U_{Fe}$ ) used in this work.

C-rate	Current density (mA cm <sup>-2</sup> ) <sup>a</sup>	Current density (mA g <sup>-1</sup> -Fe)	Duration	$U_{Fe}$ (%)
C/5.5	10.0	230.9	10 min - 4.4 h	3-80
C/5	11.0	254.5	10 min	3.3
C/4	13.8	318.2	10 min - 3.2 h	4.2-80
C/3	18.5	425.5	10 min - 36 min	5.6-20

<sup>a</sup>The cell surface area is the effective area of electrodes, 1.27 cm<sup>2</sup>.

**Table S2.** Comparison of performance of SOIARB with MOF-derived iron oxide as ESU materials with the reported results.

T (°C)	ESU materials	Current density (mA cm <sup>-2</sup> )	Duration (min)	$U_{Fe}$ (%)	Cycle number	Discharge specific energy (Wh kg <sup>-1</sup> -Fe)	RTE (%)	Ref.
500	MOF-derived Fe <sub>2</sub> O <sub>3</sub>	10.0	10	3	50	35.6	71.2	This work
		13.8	60	20	30	226.5	65.4	
		13.8	120	50	12	214.8	56.4	
		18.5	36	20	14	548.8	58.1	
500	Pd-impregnated Fe <sub>2</sub> O <sub>3</sub> -ZrO <sub>2</sub>	10.0	10	3.1	50	38.1	76.7	6
		10.0	10	3.1	500	36.7	68.5	
		10.0	159	50	25	593.4	62.9	
		11	60	21	50	238.6	67.8	
		18.5	30	21	10	228.9	59.9	
550	Fe <sub>2</sub> O <sub>3</sub> -ZrO <sub>2</sub> 10%Fe infiltrated ZrO <sub>2</sub>	10	120	-	10		40.5	7
		10	120	-	10		59.9	
		10	10	-	10		82.5	
550	Fe-ZrO <sub>2</sub>	10	10	-	10		83.3	8
					100		76.3	
650	Fe <sub>2</sub> O <sub>3</sub> -ZrO <sub>2</sub>	50	10	-	100		55.5	9

## References

- 1 Y. Xiao, X. Guo, H. Huang, Q. Yang, A. Huang and C. Zhong, *RSC Adv.*, 2015, **5**, 7253.
- 2 X. Xu, R. Cao, S. Jeong and J. Cho, *Nano Lett.*, 2012, **12**, 4988.
- 3 X. Jin, X. Zhao, C. Zhang, R. E. White and K. Huang, *Electrochim. Acta*, 2015, **178**, 190.
- 4 C. Zhang and K. Huang, *J. Power Sources*, 2017, **342**, 419.
- 5 B. C. Nguyen, T. A. Lin and D. M. Mason, *J. Electrochem. Soc.*, 1986, **133**, 1807.
- 6 C. Zhang and K. Huang, *ACS Energy Lett.*, 2016, **1**, 1206.
- 7 X. Zhao, Y. Gong, X. Li, N. Xu and K. Huang, *J. Electrochem. Soc.*, 2013, **160**, A1241.
- 8 X. Zhao, X. Li, Y. Gong and K. Huang, *Chem. Commun.*, 2014, **50**, 623.
- 9 X. Zhao, Y. Gong, X. Li, N. Xu and K. Huang, *J. Electrochem. Soc.*, 2013, **160**, A1716.